

Development and Verification of a High-Fidelity Computational Fluid Dynamics Model of Canine Nasal Airflow

Brent A. Craven
Department of Mechanical and Nuclear
Engineering,
Gas Dynamics Laboratory,
Pennsylvania State University,
University Park, PA 16802;
Computational Mechanics Division,
Applied Research Laboratory,
Pennsylvania State University,
University Park, PA 16802
e-mail: bac207@psu.edu

Eric G. Paterson
Computational Mechanics Division,
Applied Research Laboratory,
Pennsylvania State University,
University Park, PA 16802

Gary S. Settles

Michael J. Lawson

Department of Mechanical and Nuclear
Engineering,
Gas Dynamics Laboratory,
Pennsylvania State University,
University Park, PA 16802

The canine nasal cavity contains a complex airway labyrinth, dedicated to respiratory air conditioning, filtering of inspired contaminants, and olfaction. The small and contorted anatomical structure of the nasal turbinates has, to date, precluded a proper study of nasal airflow in the dog. This study describes the development of a high-fidelity computational fluid dynamics (CFD) model of the canine nasal airway from a three-dimensional reconstruction of high-resolution magnetic resonance imaging scans of the canine anatomy. Unstructured hexahedral grids are generated, with large grid sizes $((10-100) \times 10^6$ computational cells) required to capture the details of the nasal airways. High-fidelity CFD solutions of the nasal airflow for steady inspiration and expiration are computed over a range of physiological airflow rates. A rigorous grid refinement study is performed, which also illustrates a methodology for verification of CFD calculations on complex unstructured grids in tortuous airways. In general, the qualitative characteristics of the computed solutions for the different grid resolutions are fairly well preserved. However, quantitative results such as the overall pressure drop and even the regional distribution of airflow in the nasal cavity are moderately grid dependent. These quantities tend to converge monotonically with grid refinement. Lastly, transient computations of canine sniffing were carried out as part of a time-step study, demonstrating that high temporal accuracy is achievable using small time steps consisting of 160 steps per sniff period. Here we demonstrate that acceptable numerical accuracy (between approximately 1% and 15%) is achievable with practical levels of grid resolution ($\sim 100 \times 10^6$ computational cells). Given the popularity of CFD as a tool for studying flow in the upper airways of humans and animals, based on this work we recommend the necessity of a grid dependence study and quantification of numerical error when presenting CFD results in complicated airways. [DOI: 10.1115/1.3148202]

Keywords: nasal airflow, canine olfaction, 3D reconstruction, CFD verification

1 Introduction

Due to the geometric complexity of the nasal airway labyrinth, experimental investigation of the internal nasal aerodynamics is difficult. Flow visualization experiments have been reported for the human [1–6], baboon [7], monkey [8,9], rat [8,9], rabbit [10], cat [10], and dog [10,11]. In all cases, the results must be carefully interpreted given the experimental methodology. For instance, Dawes [10] used cigarette smoke to visualize the inspiratory and expiratory airflow patterns in simplified two-dimensional sagittal sections of the (highly three-dimensional) canine nasal airway. Other visualization techniques [11] infer nasal airflow patterns from the deposition of aerosols and particles, which are not neutrally buoyant and tend to impact, rather than follow the flow through convoluted airways. Water-dye flow visualization methods (e.g., Refs. [4,8,9]) have been most successful at demonstrating nasal airflow patterns.

Quantitative experimental measurements of internal nasal airflow have apparently only been made in the human [4,12–14] and baboon [7]. The more convoluted nasal passages of most keenscented (macrosmatic) animals have prevented detailed experimental airflow measurements using traditional techniques (ther-

mal anemometry, particle image velocimetry, etc.). Though newer magnetic resonance imaging (MRI) flow measurement techniques [15–20] show some promise, presently computational fluid dynamics (CFD) is the preferred method of obtaining regional distributions of velocity and temperature or mass concentration in the nasal airways of various species.

By numerically solving the governing Navier–Stokes equations on a computational grid representing the nasal airway geometry, airflow patterns in the human, monkey, and rat nose have been reported in studies of respiratory air conditioning [21–23], inhalation toxicology [24–29], and olfaction [30–35]. Computing airflow solutions in the human nose becomes difficult at high physiological airflow rates, when the physics of turbulence must be modeled. Alternatively, laminar-flow solutions in the more convoluted nose of the rat require the generation of a very elaborate computational grid. Nevertheless, the turbinate scrolls of the rat are much simpler than the branched maxilloturbinate of most carnivores (see Ref. [36]), making grid generation for nasal airflow simulations in these animals even more challenging. To date, a detailed study of the airflow in the complex nasal cavity of a macrosmatic carnivore has never been done. Consequently, the internal aerodynamics of the nose and the implications for respiratory air conditioning and olfaction in these species is not well understood.

In any CFD calculation, the fidelity of the solution depends on both the numerical method and the computational grid employed. The inherent numerical error of a particular CFD discretization

Contributed by the Bioengineering Division of ASME for publication in the JOURNAL OF BIOMECHANICAL ENGINEERING. Manuscript received July 25, 2008; final manuscript received March 24, 2009; published online August 4, 2009. Review conducted by David A. Steinman.

scheme is given by its formal order of accuracy. Given practical levels of grid resolution, first-order numerical methods often yield smooth convergent CFD solutions that are typically erroneous and corrupted by artificial dissipation. Higher-order methods of at least second-order accuracy are more acceptable and are generally required to obtain a physically-realistic numerical solution suitable for archival publication [37]. Unfortunately, although some of the more rigorous CFD studies of nasal airflows (e.g., Refs. [38–44]) report the formal order of accuracy of their numerical methods, many studies fail to include this vital information.

Grid style, resolution, and quality also contribute to numerical accuracy. Ideally, structured hexahedral grids are desirable due to their orthogonality, highly controlled grid refinement, and high inherent numerical accuracy. Nonetheless, the geometric complexity of many biological systems precludes the use of a structured grid. As shown by Longest and co-workers [43,44], for a relatively simple bifurcating geometry representative of segmental bronchi in the lung, higher numerical accuracy is achievable with structured hexahedral grids than with unstructured tetrahedral or prismatic grids and various unstructured tetrahedral-based hybrid schemes. Unstructured hexahedral grids, however, were demonstrated to yield similar solution fidelity as the structured hexahedral configuration [44].

Regardless of mesh style, high grid densities are required to resolve near-wall gradients, secondary flows, and other small-but-important solution features. Analogously, in transient calculations the temporal accuracy is a function of the time-step size. Grid quality metrics such as cell skewness, aspect ratio, and smoothness affect numerical accuracy, albeit to a lesser degree since grid quality may be optimized during grid generation.

For highly convoluted geometries such as nasal airways, geometric preservation during grid generation introduces another potential source of error. Excessively coarse computational grids fail to capture intricate geometric features, such as curvature, resulting in highly faceted surface grids that poorly represent the original geometry. As the grid resolution increases, the original geometry is more faithfully captured and is exactly recovered in the limit when the surface grid resolution equals the geometric resolution of the original surface model.

Overall, since the aforementioned errors are not independent, the cumulative numerical error must be assessed by a grid convergence study (and a time-step study for transient calculations) based on the generalized theory of Richardson extrapolation [45], as first demonstrated for respiratory airflows by Longest and co-workers [43,44]. Using a previously-verified and validated code does not guarantee an accurate solution when applied to a new problem; new calculations must be verified via a grid convergence study, which requires solutions over a range of grid resolutions to band the numerical error of the calculation [37,45]. Indeed, a single calculation on a fixed grid is unacceptable since the numerical error is indeterminable [46]. Though a number of CFD studies (e.g., Refs. [30,32,35,38,39,41]) of flow in the upper airways of various animals report grid-independent results, few studies [40,42–44] have rigorously demonstrated grid convergence and none has considered the geometric complexity of the canine nasal airway, Fig. 1.

The canine nasal cavity is divided by the nasal septum into two bilaterally-symmetric airways, each comprised of three main anatomical regions: the nasal vestibule, maxilloturbinate region, and ethmoidal region. The vestibule is the most rostral part of the nasal fossa and is primarily responsible for distributing inspired air within the nasal cavity and for directing the expired air stream [47]. The maxilloturbinate region consists of a branched bony structure (the maxilloturbinate) and numerous interconnected, highly tortuous respiratory airways, where warming or cooling, humidifying, and filtering of inspired air occurs prior to its entering the lower respiratory tract. Of the four types of maxilloturbinate found in the mammalian nasal cavity (single-scroll, double-scroll, folded, and branching), the branched maxilloturbinate is

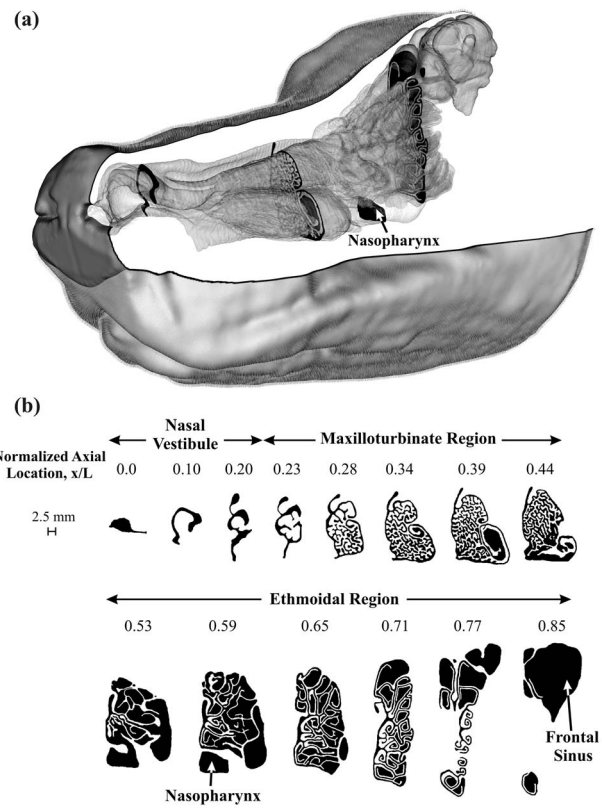


Fig. 1 Anatomy of the canine nasal airway. (a) Three-dimensional surface model of the reconstructed left nasal airway in situ. (b) Transverse airway cross sections at various axial locations.

the most convoluted and provides the greatest possible surface area for the transfer of heat and moisture [36,47]. Moving caudally, the ethmoidal region consists of a series of bony scrolls, having a “rolled-up” appearance, that provide a large surface area for olfactory mass transfer. Finally, the frontal sinuses are large recesses with no outlet located in the rear of the nasal cavity, dorsocaudal to the ethmoidal region (see Fig. 1 and Ref. [47]).

2 Objective

The objective of this study is to demonstrate the development of a high-fidelity computational model of the canine nose and verified CFD solutions of canine nasal airflow. A rigorous grid convergence study is shown, illustrating a methodology for verification of CFD calculations on complex, unstructured grids, especially in the airways of the nasal cavity.

3 Computational Methodology

The present study began with an anatomically correct, three-dimensional surface model of the left nasal airway of a 29.5 kg female Labrador retriever mixed-breed canine cadaver, which was reconstructed from high-resolution ($180 \times 180 \times 200 \mu\text{m}^3$) MRI scans [47]. The full three-dimensional geometry was utilized because preliminary reduced-order models of the canine nasal cavity failed to capture essential anatomical features of the highly three-dimensional nasal airway labyrinth (see Ref. [47]). Lumped-parameter single-path models (e.g., Refs. [48,49]) require knowledge of the airflow path, which is not obvious in the canine nasal cavity, particularly within the recessed ethmoidal region. Likewise, simplified “noselike” models designed to reproduce the general anatomy of the nasal cavity (e.g., Refs. [50–53]) failed to preserve the highly three-dimensional connectivity of critical na-

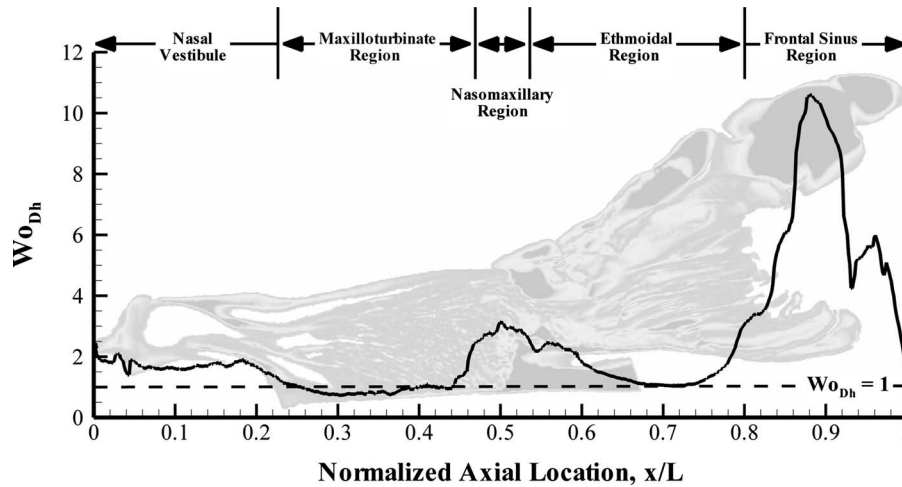


Fig. 2 Axial distribution of the Womersley number in the canine nasal cavity during sniffing ($f=5$ Hz). For reference, the background shows an appropriately scaled sagittal section of the canine nasal airway from Ref. [47].

sal airway regions. Consequently, development of a three-dimensional anatomically-accurate CFD model was required.

3.1 Assumptions. The CFD calculation assumes that the bony internal turbinate structures of the canine nasal cavity are rigid. A static undilated nostril is modeled here. Including physiologically realistic nostril motion would be interesting, but has yet to be fully defined for the canine. The influence of naris motion is the subject of future work and is not expected to affect the general results and conclusions of this study.

Based on detailed morphometric airway data from the same nasal cavity [47] and recent experimental measurements of canine sniffing [54], the regional distribution of the nondimensional Womersley and Reynolds numbers were calculated from Eqs. (1) and (2), respectively. Here, f is the sniff frequency in units of hertz, Q^{peak} is the peak inspiratory airflow rate, ν is the kinematic viscosity of air, and D_h and A_c are, respectively, the local airway hydraulic diameter and cross-sectional area. From allometric scaling of the experimental data, the peak inspiratory airflow rate of a sniff for a 29.5 kg canine is about 0.4 l/s per nostril, while the sniff frequency is roughly 5 Hz, independent of body size [54].

$$Wo_{D_h} = \frac{D_h}{2} \sqrt{\frac{2\pi f}{\nu}} \quad (1)$$

$$Re_{D_h}^{\text{peak}} = \frac{Q^{\text{peak}} D_h}{A_c \nu} \quad (2)$$

Figure 2 shows the axial distribution of the Womersley number in the reconstructed model of the canine nasal cavity. Physically, the magnitude of the Womersley number is an indicator of the degree of unsteadiness in the flow [55]. In general, when $Wo_{D_h} < 1$ the flow may be approximated as quasisteady, permitting steady-state solution of the governing Navier–Stokes equations. However, as the Womersley number grows larger than unity, the flow increasingly deviates from quasisteady behavior, eventually leading to fully unsteady flow phenomena such as the formation of Stokes layers on the airway walls [56]. From Fig. 2, the canine nasal cavity contains both regions of high- and low-Womersley number flows, indicating that the overall unsteadiness of canine nasal airflow during sniffing is unknown *a priori*. Consequently, in contrast to humans [30,32], monkeys [27], and rats [33,35], canine sniffing must be modeled as fully transient in the present CFD study.

Phenomenologically, the nature of the flow (whether laminar or turbulent) depends on the existence of either quasisteady or unsteady flow phenomena. For quasisteady laminar pipe flow, the

well-known parabolic velocity profile becomes unstable and transition to turbulence occurs in the 2000–4000 Reynolds number range [57,58]. Fully unsteady flow may be characterized by the ratio of the peak oscillatory Reynolds number to the Womersley number, $Re_{D_h}^{\text{peak}}/Wo_{D_h}$. If $Wo_{D_h} > 1$, then transition to turbulence in oscillatory pipe flow occurs when this ratio is between approximately 250 and 1000 [59]. Although airway curvature and branching affect the stability of the flow [60], these nondimensional parameters provide at least a rough indication of the nature of canine nasal airflow during sniffing.

Based on this, Fig. 3 shows a map of the anticipated flow regimes within the nasal cavity at peak inspiration. Depending on the magnitude of the Womersley number, the axial distribution of the appropriate nondimensional parameter ($Re_{D_h}^{\text{peak}}/Wo_{D_h}$ or $Re_{D_h}^{\text{peak}}$) is plotted from the naris to the nasopharynx. Estimates beyond the nasopharynx are not shown due to insufficient *a priori* knowledge of the velocity distribution in the recessed ethmoidal and frontal sinus regions. In the nasal vestibule, where $Wo_{D_h} > 1$, the ratio of the peak Reynolds number to the Womersley number indicates that the airflow is turbulent there at peak inspiration. Downstream of the nasal vestibule, where $Wo_{D_h} < 1$, relaminarization is expected to occur and low-Reynolds-number ($Re_{D_h}^{\text{peak}} \sim 100$) quasisteady laminar airflow is expected.

The most straightforward approach to simultaneously calculate laminar, transitional, and turbulent flows in the convoluted canine nasal cavity is by direct numerical simulation (DNS). Spatial and temporal resolution requirements for DNS of this complicated flowfield may be approximated from turbulence theory (see Refs. [61–63]). A conservative estimate of the finest DNS grid and time-step resolution required to capture the smallest turbulent eddies is found to be $\eta=5 \mu\text{m}$ and $\tau_{\eta}=1 \mu\text{s}$ [54], respectively.

Alternatively, the two-equation low-Reynolds-number $k-\omega$ turbulence model of Wilcox [64] has been used with some success on transitional hemodynamic flows [65,66]. Though, a recent study by Varghese et al. [67] comparing the performance of various turbulence models at predicting poststenotic transition to turbulence with DNS [68] concluded that many widely used models, including the low-Reynolds-number $k-\omega$ model and a large-eddy simulation (LES) model, were not able to capture transitional phenomena. An adaptation of the Wilcox model [69,70] and the two-equation $q-\zeta$ model [71] have been more successful at simulating multiregime internal flows, including pulsatile transition and relaminarization.

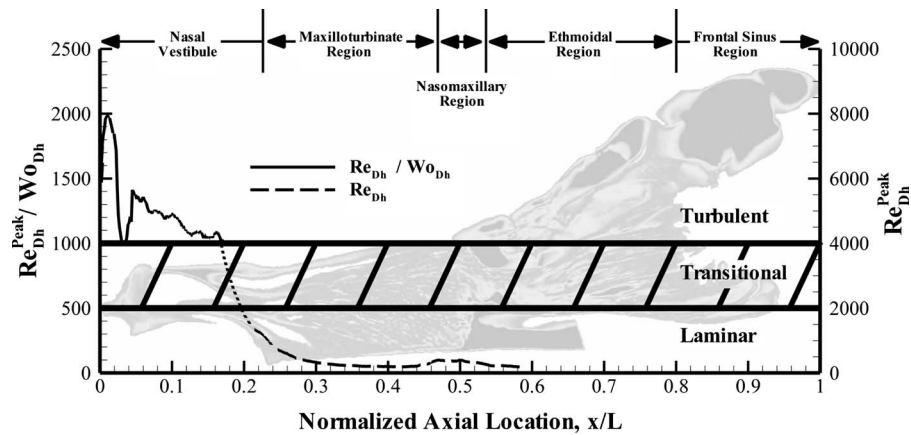


Fig. 3 Nature of canine nasal airflow during sniffing

Nonetheless, the present study is primarily focused on laminar airflow in the maxilloturbinate and ethmoidal regions. Since transitional and turbulent flow is confined to the nasal vestibule and does not exist throughout the entire sniff cycle (at lower instantaneous sniff airflow rates), the difficulty and ambiguity of modeling pulsatile transition and relaminarization are not presently warranted. Thus, here the effect of periodic turbulent flow in the vestibule is neglected and laminar airflow is calculated through the entire nasal cavity. Given the occurrence of low-Reynolds-number (~ 100) laminar airflow in the maxilloturbinate region (see Fig. 3), we do not expect the advection of turbulence to significantly affect the solution downstream of the nasal vestibule. Even so, the role of pulsatile turbulence and regional mixing in the vestibule of the canine nasal cavity is the subject of future work.

Lastly, this study assumes that the airway secretions that cover most of the nasal airways (see Ref. [47] for discussion) may be neglected. According to Proctor [72], the flow of mucus along the airway epithelial surface is quite slow, on the order of 1 cm/min, and is primarily due to mucociliary transport. Due to the small relative thickness of the aqueous “mucus” layer ($\sim 10 \mu\text{m}$ [73–75]) compared with the dimensions of the smallest airways ($\sim 1 \text{ mm}$) and its liquid composition, airway secretions have a negligible influence on the internal aerodynamics.

3.2 Boundary Conditions. Due to bilateral symmetry and complete separation of the left and right canine nasal cavities, only flow in the left nasal airway is computed here. As shown in Fig. 4, the computational domain consists of the reconstructed left nasal airway and the entire external nose, merged with a separate reconstructed surface model of the external cranial anatomy (see Ref. [47]) and placed in a large rectangular “box,” where farfield atmospheric pressure boundary conditions are specified. Preliminary two-dimensional computations were used to optimize the size of the farfield computational boundary to avoid inflow and outflow boundary effects on inspiratory and expiratory airflow at the naris, respectively. An optimal minimum farfield boundary distance was found to be roughly 25 narial diameters from the left nostril.

Consequent of the neglect of the nasal mucus layer and its influence on the internal aerodynamics, no-slip boundary conditions were applied on all solid surfaces of the canine nose and head. Nasopharynx pressure outlet and inlet boundary conditions were specified such that inspiratory and expiratory airflow rates and sniff frequency roughly matched experimental values [54]. Computations of steady inspiration and expiration used a constant nasopharyngeal pressure, whereas transient simulations of sniffing used a 5 Hz sinusoidal nasopharyngeal pressure boundary condition.

3.3 Grid Generation. The complicated geometry of the canine nasal cavity required an unstructured grid generation scheme. A semi-automated octree-based method (Harpoon, Sharc Ltd., Manchester, UK) was used to generate both unstructured hexahedral and tetrahedral grids by assigning separate surface cell sizes to different geometric parts and an overall grid expansion ratio. For variable hexahedral grid refinement, hanging vertices were removed and wedges, pyramids, and tetrahedra were used as buffer cells between regions of fine and coarse hexahedra. Grid quality was optimized as a postprocessing step via a skewness-based smoothing algorithm [76], where maximum grid skewness was improved by smoothing computational cells exceeding a target skewness value of approximately 0.9. Multiple smoothing iterations were performed to best improve grid quality.

A critical preliminary step for grid generation was the splitting-up of the external geometry and nasal airway into multiple surface parts, which permitted regional specification of grid resolution. Since a coarse-grid density may be used in the farfield and gradually refined in the vicinity of the head and nose, the farfield boundary and the external head and nose were all separately defined. As shown in Fig. 5, multiple internal surfaces were defined, permitting variable nasal airway grid refinement. Particularly, fine-grid resolution is required in the main airway regions (e.g., nasal vestibule, maxilloturbinate, and ethmoidal regions),

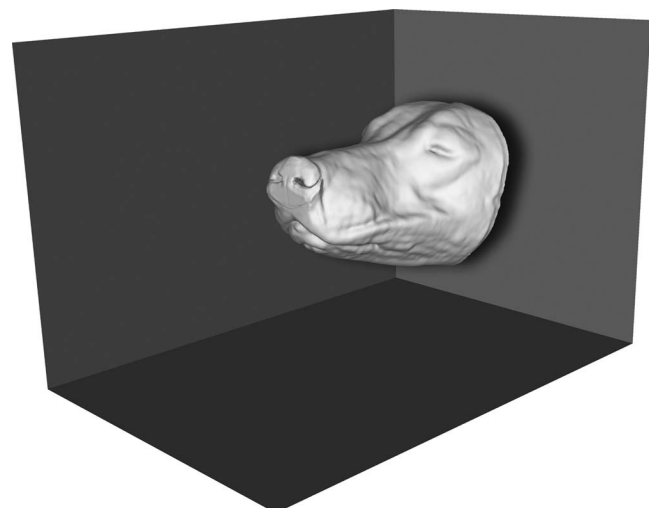


Fig. 4 Computational domain

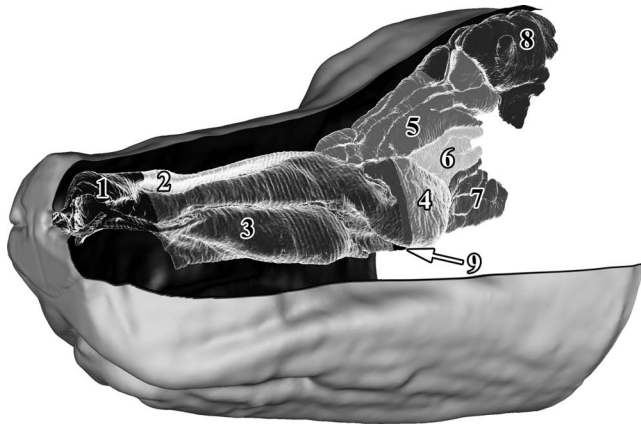


Fig. 5 Regional division of the internal nasal airway surfaces for variable CFD grid refinement. Regions include the nasal vestibule (1), dorsal meatus (2), maxilloturbinate region (3), maxillary sinus (4), ethmoturbinate region ((5)–(7)), frontal sinus (8), and nasopharynx (9).

whereas a relatively coarser grid may be used in the frontal and maxillary sinuses, where low-velocity or stagnant airflow not actively involved in sniffing is anticipated.

Even with variable grid refinement, in order to capture the gross geometry of the small airways in the maxilloturbinate and ethmoidal regions, the coarsest permissible grid contained nearly 14×10^6 computational cells. Coarser grid resolutions failed even to capture the smallest airways; these airways were effectively filtered out by the octree method when the assigned surface cell size was roughly equivalent to the smallest airway diameter. Furthermore, due to the geometric complexity of the nasal airways, the use of a near-wall grid was not possible. Near-wall grid generation failed in highly-tortuous airway regions, resulting in collapsed and highly-skewed near-wall layers and a corrupted CFD model.

As shown in Fig. 6(a), a power-law relationship between the total number of computational cells and the specified surface cell size was found for both the hexahedral and tetrahedral grid generation schemes. The difference from uniform isometric scaling is attributable to nonuniform refinement in the external domain and, internally, in the frontal and maxillary sinuses. Isometric scaling refers to geometric similarity, and is used here to describe the relationship ($N \sim \Delta x^{-3}$) between the number of computational cells, N , in a uniform-grid domain and the constituent cell size, Δx . Clearly, the approach of splitting up the computational model for regional grid refinement produced smaller overall grids than otherwise obtained via a uniform refinement approach.

Comparing hexahedral and tetrahedral grid generation schemes, for a given surface cell size tetrahedral grids contained three to four times the number of computational cells than the equivalent hexahedral grid. Given that hexahedral grids are also more accurate than tetrahedral grids with the same effective spatial resolution [43,77], the former mesh style was chosen for CFD computations of canine nasal airflow.

Four hexahedral grids were used for a rigorous grid refinement study. Table 1 contains a summary of the total number of computational cells in each grid and the specified surface cell size and spatial resolution in the main airway regions of each model. The coarsest grid contained roughly 14×10^6 cells. Finer CFD grids were obtained by judiciously assigning a surface cell size to achieve an overall grid doubling, resulting in medium and fine grids having approximately 28×10^6 and 54×10^6 computational cells, respectively. The finest-grid resolution was limited by practical computational requirements for numerical solution. From Fig. 6(b), the largest grid contained roughly 104×10^6 computational cells and required nearly 30 Gbytes of memory to generate.

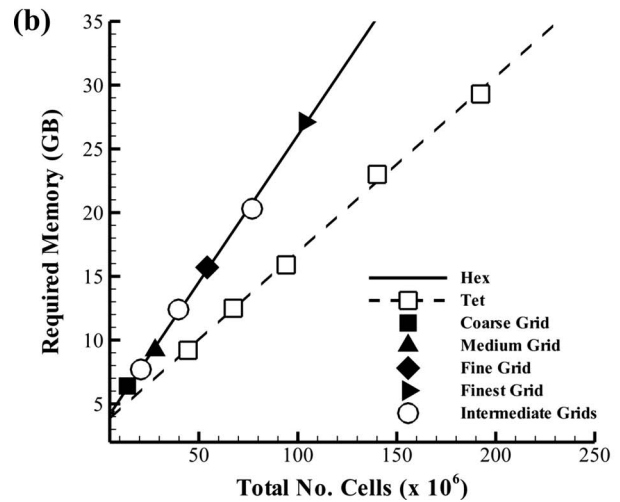
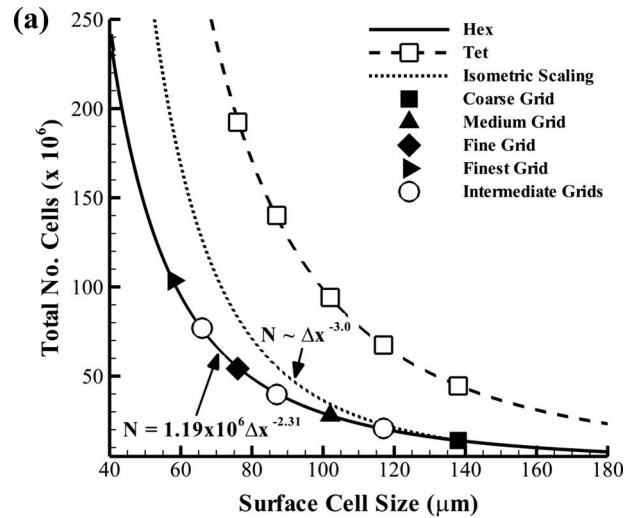


Fig. 6 Comparison of hexahedral and tetrahedral unstructured grid generation. (a) Overall grid size versus assigned surface cell size, Δx , in the main canine nasal airway regions. (b) Required computer memory for grid generation versus overall grid size. Grids shown by open symbols were generated to develop the power-law (a) and linear (b) regressions.

Even so, the specified surface cell size in the main airways was $58 \mu\text{m}$, far too coarse for DNS of transition and turbulence in the nasal vestibule.

A summary of the external grid is shown in Fig. 7 for the fine-grid CFD model. The resolution is coarse, except within a hemispherical refinement region encompassing the external nares, where sufficient grid density is required to resolve the expiratory

Table 1 Summary of the coarse, medium, fine, and finest unstructured hexahedral grids

Grid	Total No. computational cells ($\times 10^6$)	Surface cell size (μm)	Spatial resolution ^a (No. of cells/airway diameter)
Coarse	13.9	138	3–5
Medium	27.9	102	4–6
Fine	54.2	76	5–7
Finest	103.6	58	6–8

^aRepresentative spatial resolution within the smallest, most convoluted airways of the nasal cavity (in the maxilloturbinate region).

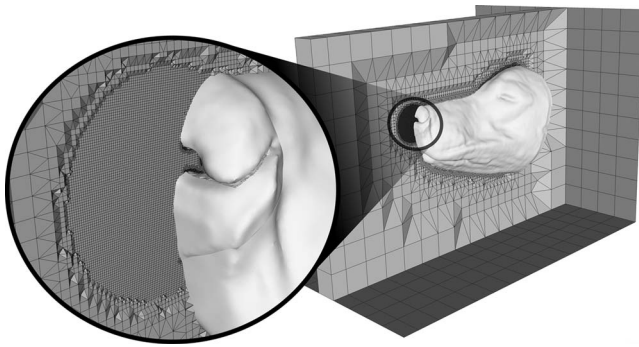


Fig. 7 External grid summary of the fine CFD model

air jet. Overall, the external domain contained roughly 2–3% of the total number of computational cells in each grid.

In Fig. 8, a comparison of the internal grid density is shown for the four grids within the small and tortuous airways of the maxilloturbinate region, the most convoluted part of the nasal cavity. Here, the spatial resolution of the coarse, medium, fine, and finest CFD grids is roughly 3–5, 4–6, 5–7, and 6–8 computational cells per airway diameter, respectively.

3.4 Numerical Methods. A second-order accurate Galerkin least-squares (GLS) finite element method [78–81] (AcuSolve, ACUSIM Software, Inc., Mountain View, CA, USA) was used to numerically solve the incompressible Navier–Stokes equations via a fully-coupled Krylov subspace iterative solver, based on the generalized minimal residual (GMRES) method. For steady-state solution, a first-order-accurate implicit Euler integration algorithm

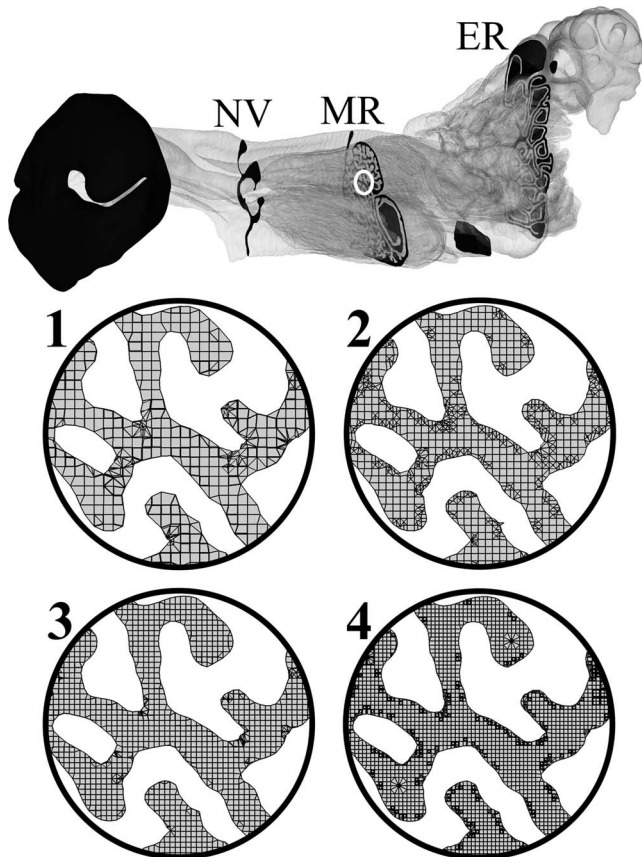


Fig. 8 Comparison of the internal spatial resolution of the (1) coarse, (2) medium, (3) fine, and (4) finest CFD grids in the maxilloturbinate region (MR). Comparable grid resolution is found in the nasal vestibule (NV) and ethmoidal region (ER).

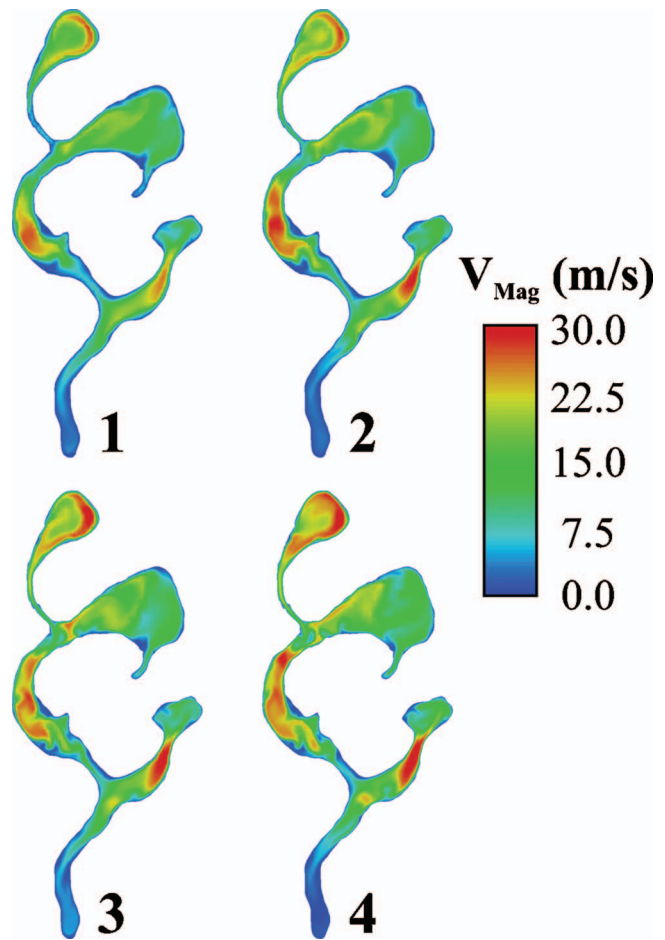


Fig. 9 Qualitative comparison of the velocity distribution in the nasal vestibule (NV) for the (1) coarse-, (2) medium-, (3) fine-, and (4) finest-grid solutions of inspiratory airflow for an overall pressure drop of 2000 Pa

was utilized, whereas a second-order-accurate time integration scheme (Gear’s method) was used for transient calculations of sniffing. Iterative convergence was guaranteed by forcing the normalized residuals and solution increments of pressure and velocity to be less than 10^{-5} . Reduction in the convergence criterion to 10^{-6} had a negligible influence on the solution. Furthermore, various solution variables were monitored throughout the simulation to ensure convergence of the computed result.

Computations were performed on a parallel computer cluster at Penn State University consisting of 256 2.8 GHz Intel Xeon processors with 2 Gbytes of memory per processor. Depending on the grid size, 26–120 processors were utilized in steady-state calculations that required between 4 h and 30 h of wall clock time. Transient calculations performed on 100 processors consumed between 70 h and 90 h of wall clock time, depending on the time-step size. In all, the computations presented herein required approximately 73,000 CPU hours and consumed about 820 h of wall clock time.

4 Results

4.1 Grid Dependence Study. The qualitative features of the CFD solutions for all of the grids are remarkably consistent. For a given pressure drop, similar velocity distributions, pressure contours, and overall flow patterns were obtained, regardless of grid resolution. Figure 9 illustrates the qualitative comparison of the velocity distribution in the nasal vestibule for the various grid solutions. Here, the highest computed velocities occur in compa-

rable locations and similar gross secondary flow features are observed in each case. Similar qualitative comparisons apply throughout the nasal cavity. Thus, the overall kinematics of canine nasal airflow is reasonably well captured, even in the coarse-grid solution.

A subtle, yet important, qualitative difference between solutions from different grids is the size of the smallest observed flow structures. Smaller scales of motion are resolved by finer grids, especially for airflow in the nasal vestibule (Fig. 9), where the highest Reynolds numbers occur (see Fig. 3). Theoretically, for turbulent flow in the vestibule, further grid refinement would resolve smaller and smaller flow scales, until the smallest Kolmogorov eddies are captured by direct numerical simulation. Nonetheless, the largest scales of motion, which are resolved, contain most of the kinetic energy and determine the bulk fluid motion and overall kinematics of airflow in the vestibule. Conversely, downstream low-Reynolds-number laminar mixing occurs exclusively on a length scale of order D_h , resulting in fewer unresolved small-scale flow features in the coarse-grid solutions.

Quantitatively, airflow “impedance” curves of overall pressure drop versus flow rate were used to examine grid dependency. Such curves are typically used to characterize resistive systems of fluid flow driven by fans or blowers. This particular measure is appropriate because it quantifies the sum of frictional pressure drop and “minor” losses due to flow separation and mixing (see Ref. [57]), which are both significant in the present geometry. Moreover, it is directly comparable to experimental data.

In all, 46 steady-state solutions were calculated in order to develop the inspiratory and expiratory airflow impedance curves, Figs. 10(a) and 10(b), respectively. In general, a nonlinear trend in pressure drop is observed. This is characteristic of internal flows with mixing and secondary motions known as minor losses, which increase nonlinearly with airflow rate.

Both inspiratory and expiratory airflow impedance curves exhibit monotonic convergence with grid refinement. For a given pressure drop, the airflow rate is shown to increase and to monotonically approach a presumed exact theoretical solution with increasing grid resolution, Fig. 11. Furthermore, grid dependence of the solution is a function of the overall pressure drop; a larger range of calculated airflow rates is obtained at larger pressure drops.

To investigate the observed increase in overall airflow rate with grid refinement at a constant pressure drop, the regional distribution of airflow in the nasal cavity was considered. Specifically, the fraction of the overall airflow passing through the dorsal meatus was extracted from each of the grid solutions and compared at various axial locations for an overall pressure drop of 2000 Pa. The results for inspiration and expiration are shown in Figs. 12(a) and 12(b), respectively.

During inspiration, most of the pressure losses in the rostral part of the nasal cavity are due to minor losses associated with mixing and the formation of secondary flows as air at a comparatively high velocity flows through the nasal vestibule and enters the branched airways of the maxilloturbinate region. The dorsal meatus, however, is an effective bypass around this complicated airway region. In the CFD calculations, with grid refinement smaller-scale flow structures and mixing are increasingly resolved in this region, leading to an increase in flow resistance for air entering the maxilloturbinate airways. Consequently, proportionally more airflow takes the path of less resistance via the dorsal meatus, around the rostral part of the maxilloturbinate region of the nasal cavity (see Fig. 12(a)).

Downstream, however, the opposite effect of grid resolution on airflow in the dorsal meatus is shown in Fig. 12(a). Here, low-Reynolds-number (~ 100) laminar airflow exists in the maxilloturbinate airways, which appears to be well resolved by even the coarse grid. Thus, increasing the grid resolution has little effect on the airflow resistance in these airways. However, the dorsal meatus contains higher-velocity airflow and grid refinement results in

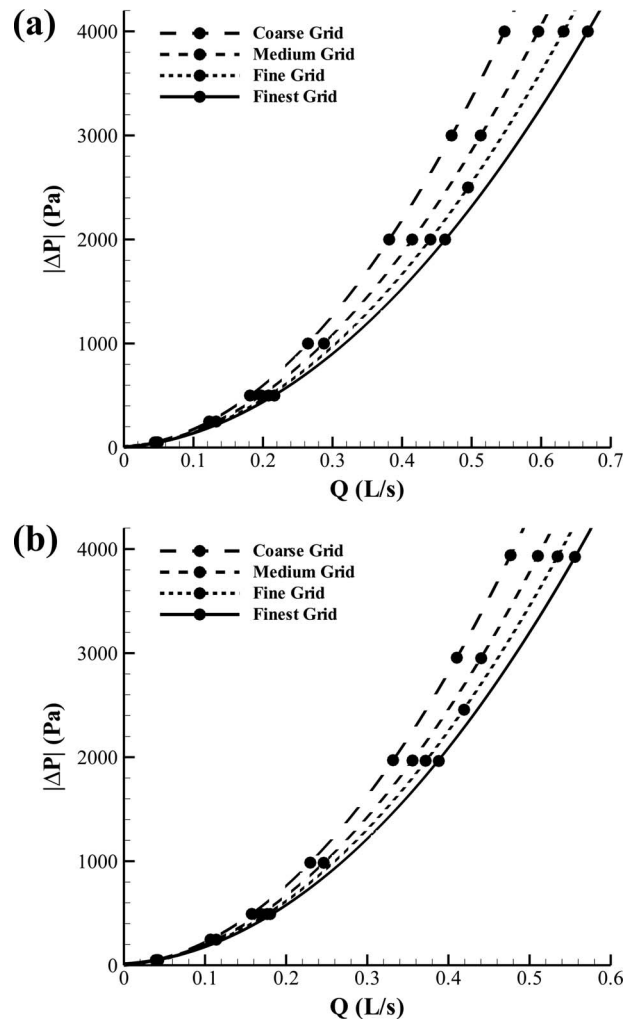


Fig. 10 Airflow “impedance” curves, a quantitative measure of grid dependence for CFD calculations of (a) inspiratory and (b) expiratory airflows in the canine nasal airway

increased resolution of shear stress and frictional losses in this airway. Thus, as grid resolution increases proportionally, more airflow leaves the dorsal meatus due to increased frictional resistance and enters the maxilloturbinate airways. The same effect is observed on expiration, Fig. 12(b).

Taken together, the dynamic allocation of airflow in the nasal cavity with grid refinement results in an increase in the overall flow rate through the nose for a given pressure drop. The effect is most dramatic at high pressure drops and for inspiration, rather than expiration. For small pressure drops, the influence of grid resolution is relatively negligible.

Richardson extrapolation is the standard method for estimating numerical error in the verification of CFD calculations. The generalized theory of Richardson extrapolation requires a “consistent” numerical method and calculated solutions within the asymptotic range of convergence [45]. For unstructured grids, verification of global or integrated quantities is typically performed, since direct comparison of nodal values requires interpolating the solutions to a common grid, introducing an additional source of error. Here, Richardson extrapolation is performed on the calculated airflow rates within the physiological range during sniffing at three pressure drops ($\Delta P=50, 500, \text{ and } 2000 \text{ Pa}$) for steady inspiration and expiration.

Equations (3)–(7) summarize the theory of Richardson extrapolation. For a “consistent” numerical method, the calculated solutions, $f_i(\Delta)$, better approximate the exact solution, f_{exact} , as the

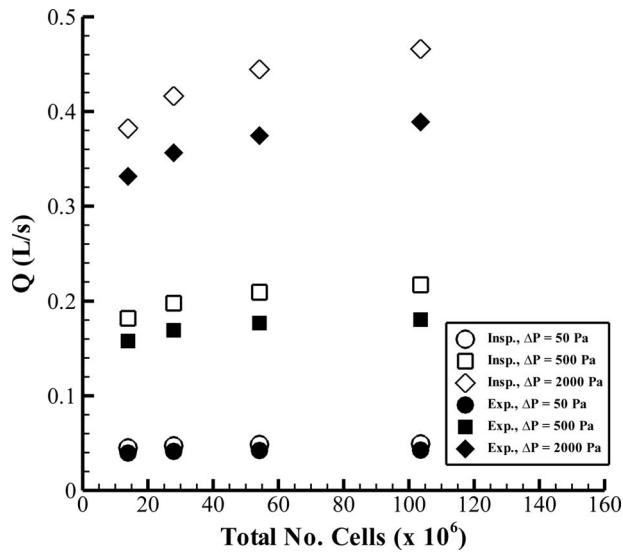


Fig. 11 Monotonic convergence of airflow rate, Q , through the canine nasal cavity from CFD calculations at various pressure drops

numerical error, $C\Delta_i^p$, decreases with grid refinement. Here, C is a coefficient, Δ is the grid spacing, and p is the observed order of convergence [45]. Numerical solutions computed on the finest (f_1), fine (f_2), and medium (f_3) grids were used to evaluate p from Eq. (4) for a constant grid refinement ratio r , Eq. (5). Although Roache [45] recommended a minimum refinement ratio of 1.1 to overcome random sources of error in the computed results (e.g., “noise” from incomplete iterative convergence), for calculations of airflow in the complicated geometry of the canine nasal cavity on unstructured grids, a larger value was required; an overall doubling of the grid size yielding $r \approx 1.24$ worked well.

The estimated fractional error of the fine-grid solution, E_1 , was evaluated from Eq. (6), where the observed order of convergence p (Eq. (4)) was used rather than the theoretical convergence rate (i.e., the formal order of accuracy of the numerical method) as is commonly done in two-grid convergence studies. The grid convergence index (GCI), originally proposed by Roache [82] and defined in Eq. (7), is a measure of the fractional error that has a high probability of bounding the actual error of the numerical solution [45]. Based on the recommendation of Roache [45], a “factor of safety,” F_s , of 1.25 was used in the present convergence study, where three grids are utilized to determine the observed order of convergence p . Alternatively, for two-grid convergence

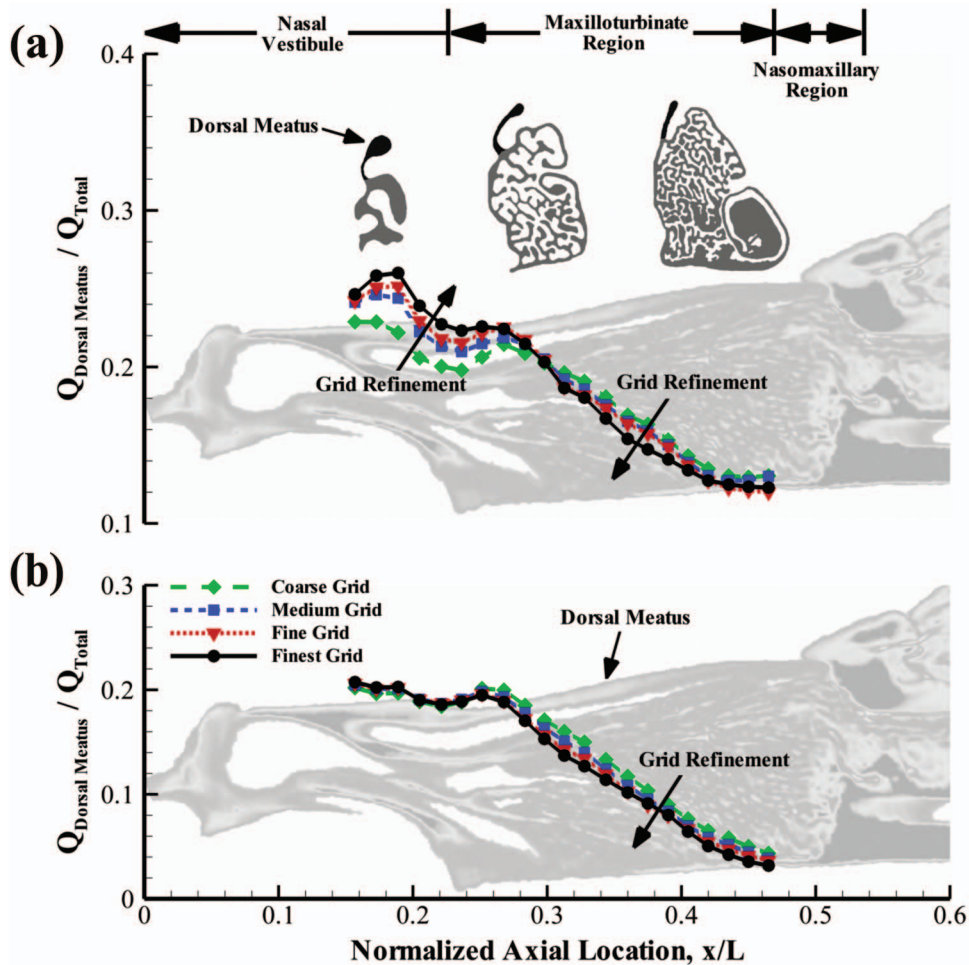


Fig. 12 Grid dependence of the regional airflow distribution in the canine nasal cavity at a pressure drop of 2000 Pa. The fraction of the overall airflow passing through the dorsal meatus during steady (a) inspiration and (b) expiration from coarse-, medium-, fine-, and finest-grid solutions is plotted at various axial locations. For reference, the background contains a sagittal section of the nasal airway and three transverse cross sections are shown at correct axial locations to illustrate the relative size and location of the dorsal meatus.

Table 2 Grid refinement study—summary of Richardson extrapolation

ΔP (Pa)	Inspiration			Expiration		
	p	E_{finest} (%)	GCI_{finest} (%)	p	E_{finest} (%)	GCI_{finest} (%)
50	4.1	-0.8	1.1	4.0	-0.7	0.8
500	1.8	-7.8	9.8	3.6	-1.7	2.2
2000	1.2	-15.1	18.8	1.1	-14.5	18.1

studies using the theoretical convergence rate in Eq. (6), a F_s of 3 is recommended [45].

$$f_i(\Delta) = f_{\text{exact}} + C\Delta_i^p \quad (3)$$

$$p = \frac{\ln\left(\frac{f_3 - f_2}{f_2 - f_1}\right)}{\ln(r)} \quad (4)$$

$$r \approx \left(\frac{N_1}{N_2}\right)^{1/3} \approx \left(\frac{N_2}{N_3}\right)^{1/3} \quad (5)$$

$$E_1 = \frac{\left(\frac{f_2 - f_1}{f_1}\right)}{r^p - 1} \quad (6)$$

$$GCI_1 = F_s |E_1| \quad (7)$$

A summary of the Richardson extrapolation analysis is given in Table 2, where E_{finest} and GCI_{finest} are the estimated percent error and grid convergence index of the finest-grid solution, respectively. At the lowest pressure drop, rapid grid convergence is demonstrated by high values of p for inspiration and expiration. As a result, the finest-grid solution is quite accurate at these low Reynolds numbers, yielding GCI values of 1.1% and 0.8% for inspiration and expiration, respectively. However, as the airflow rate and Reynolds number increase with larger pressure drops, the order of convergence decreases and the numerical error increases. At a pressure drop of 500 Pa, the GCI values are less than 10%, whereas at 2000 Pa the numerical error is in the 15% range.

4.2 Time-Step Study. Lastly, transient solutions of canine sniffing were calculated and a time-step study was performed to evaluate the temporal accuracy. Since separate convergence studies may be used to independently assess spatial and temporal error [45], for convenience the “fine” grid was used for transient calculations of sniffing at 5 Hz at physiologically realistic airflow rates. A sinusoidal nasopharynx pressure boundary condition, varying about atmospheric pressure, of amplitude 2500 Pa was used to mimic a sniff.

Four time-step sizes were used, ranging from 20 to 160 time steps per sniff period, with a constant refinement ratio of 2. To hasten convergence, all transient calculations but the first were restarted from the previous coarser time-step solution. The initial condition of the first unsteady calculation was taken from the steady-state solution for inspiration at an overall pressure difference of 2500 Pa.

Figure 13(a) shows the time history of airflow rate at the nasopharynx for all of the transient calculations of sniffing. Here, Δt is the time-step size and T is the period of a single sniff, comprised of an inspiration and an expiration. For a coarse step size of $\Delta t/T = 1/20$, nonphysical, high-frequency oscillations in flow rate occur, which is an indication that the solution is not within the asymptotic range of convergence [45]. However, when the time-step size is refined, nonphysical oscillations disappear and a smooth sinusoidally-varying airflow rate is obtained. For the finest

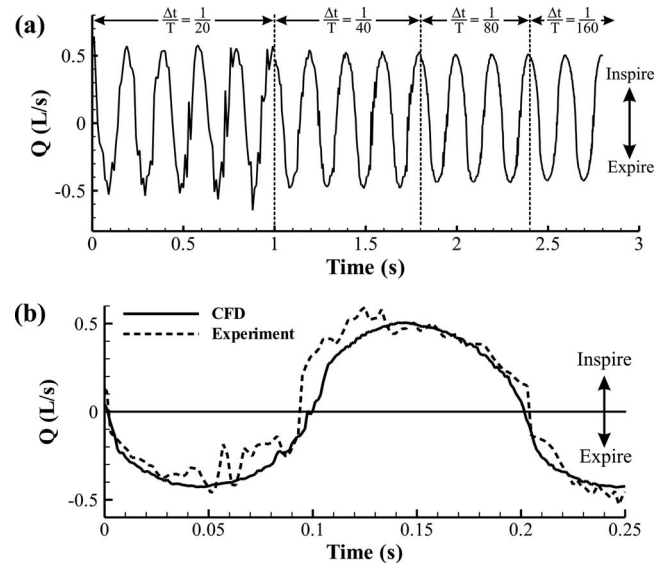


Fig. 13 Transient calculations of canine sniffing at 5 Hz. (a) Time history of airflow rate at the nasopharynx for all calculated sniffs, with decreasing time-step size. (b) Comparison of the calculated airflow rate for the finest time-step size and experimental measurements. The experimental data, originally measured on a smaller canine [54], were allometrically scaled to 29.5 kg, the body mass of the dog from which the CFD model was reconstructed.

time-step size, a comparison of the computed airflow rate with experimental measurements [54] is shown in Fig. 13(b). Excellent agreement is demonstrated.

The time accuracy of the CFD solution using the smallest time-step size was assessed by performing Richardson extrapolation on the average peak inspiratory and expiratory flow rates obtained with each of the three smallest time-step sizes. Table 3 contains a summary of the results. In both cases, the temporal order of convergence was nearly second order and the transient solutions are quite accurate, with little numerical error ($\sim 1\%$) due to time discretization. Consequently, the total numerical error in the CFD calculation, taken as the sum of the spatial and temporal errors [45], is predominately due to the spatial contribution.

5 Conclusions

A high-fidelity CFD model of the canine nasal airway was developed that required at least 14×10^6 computational cells to capture the smallest airways. In the practical limit, larger grids (up to $\sim 100 \times 10^6$ cells) were constructed and used in a rigorous CFD verification study. Numerical solutions on each of the grids were then compared to examine the grid dependence of the CFD solutions. Transient computations of canine sniffing were also performed using successively smaller time-step sizes to quantify the temporal numerical error via Richardson extrapolation.

Qualitatively, the overall features of the CFD solutions were similar, independent of grid refinement. For a given pressure drop, similar qualitative velocity distributions and overall flow patterns

Table 3 Time-step study—summary of Richardson extrapolation

p	Inspiration		Expiration	
	E_{finest} (%)	GCI_{finest} (%)	p	E_{finest} (%)
1.7	0.5	0.6	1.9	0.9

were obtained for all of the grids. Quantitative results demonstrated monotonic convergence with grid refinement, with a larger grid dependence at higher airflow rates. Furthermore, the regional distribution of airflow in the nasal cavity was shown to depend on the grid resolution. The inherent numerical error in the “finest”-grid CFD solution was evaluated using Richardson extrapolation, which showed that, at physiologically-realistic airflow rates, acceptable numerical accuracy (between approximately 1% and 15%) is achievable.

Transient computations of canine sniffing revealed that at least 40 time steps per sniff period were required to obtain a well-behaved solution. Larger time-step sizes yielded high-frequency nonphysical oscillations in the solution. The time accuracy of the smallest time-step solution was evaluated via Richardson extrapolation, which gave a small temporal numerical error (~1%).

In summary, this study demonstrates that, although the qualitative characteristics of solutions are much the same for different grids, quantitative CFD data from calculations of canine nasal airflow are moderately grid dependent. Given the popularity of CFD as a tool for studying flow in the upper airways of humans and animals, and based on our rigorous verification study, we recommend the reporting of a grid dependence study and a quantification of numerical error when presenting CFD results in these complicated airways. This is especially important when the CFD solution relates to human health.

Acknowledgment

The authors thank Chuck Ritter of the Applied Research Laboratory at Pennsylvania State University for technical assistance and the staff at Sharc Ltd. and ACUSIM Software, Inc. for their recommendations and support. We also thank J.D. Miller and L.J. Dodson of the Gas Dynamics Laboratory at Pennsylvania State University for their assistance. The authors appreciate insightful comments from two anonymous reviewers. Financial support for this work was provided by the Office of Naval Research (Grant No. N00014-05-1-0844).

References

- Paulsen, E., 1882, “Experimentelle Untersuchungen Über Die Strömungen Der Luft in Der Nasenhöhle,” *Sitzungsberichte der kaiserliche Academie der Wissenschaften, III Abteilung*, **85**, pp. 348–373.
- Proetz, A. W., 1951, “Air Currents in the Upper Respiratory Tract and Their Clinical Importance,” *Ann. Otol. Rhinol. Laryngol.*, **60**(2), pp. 439–467.
- Proetz, A. W., 1953, *Applied Physiology of the Nose*, Annals, St. Louis.
- Swift, D. L., and Proctor, D. F., 1977, “Access of Air to the Respiratory Tract,” *Respiratory Defense Mechanisms*, Marcel Dekker, New York, Chap. 3, pp. 63–93.
- Hornung, D. E., Leopold, D. A., Youngentob, S. L., Sheeche, P. R., Gagne, G. M., Thomas, F. D., and Mozell, M. M., 1987, “Airflow Patterns in a Human Nasal Model,” *Arch. Otolaryngol. Head Neck Surg.*, **113**(2), pp. 169–172.
- Simmen, D., Scherrer, J. L., Moe, K., and Heinz, B., 1999, “A Dynamic and Direct Visualization Model for the Study of Nasal Airflow,” *Arch. Otolaryngol. Head Neck Surg.*, **125**(9), pp. 1015–1021.
- Patra, A. L., Gooya, A., and Morgan, K. T., 1986, “Air-Flow Characteristics in a Baboon Nasal Passage Cast,” *J. Appl. Physiol.*, **61**(5), pp. 1959–1966.
- Morgan, K. T., and Monticello, T. M., 1990, “Air-Flow, Gas Deposition, and Lesion Distribution in the Nasal Passages,” *Environ. Health Perspect.*, **85**, pp. 209–218.
- Morgan, K. T., Kimbell, J. S., Monticello, T. M., Patra, A. L., and Fleishman, A., 1991, “Studies of Inspiratory Air-Flow Patterns in the Nasal Passages of the F344 Rat and Rhesus-Monkey Using Nasal Molds—Relevance to Formaldehyde Toxicity,” *Toxicol. Appl. Pharmacol.*, **110**(2), pp. 223–240.
- Dawes, J. D. K., 1952, “The Course of the Nasal Airstreams,” *J. Laryngol. Otol.*, **66**(12), pp. 583–593.
- Becker, R. F., and King, J. E., 1957, “Delineation of the Nasal Air Streams in the Living Dog,” *AMA Arch. Otolaryngol.*, **65**(5), pp. 428–436.
- Hahn, I., Scherer, P. W., and Mozell, M. M., 1993, “Velocity Profiles Measured for Airflow Through a Large-Scale Model of the Human Nasal Cavity,” *J. Appl. Physiol.*, **75**(5), pp. 2273–2287.
- Hopkins, L. M., Kelly, J. T., Wexler, A. S., and Prasad, A. K., 2000, “Particle Image Velocimetry Measurements in Complex Geometries,” *Exp. Fluids*, **29**(1), pp. 91–95.
- Kelly, J. T., Prasad, A. K., and Wexler, A. S., 2000, “Detailed Flow Patterns in the Nasal Cavity,” *J. Appl. Physiol.*, **89**(1), pp. 323–337.
- Elkins, C. J., Markl, M., Pelc, N., and Eaton, J. K., 2003, “4D Magnetic Resonance Velocimetry for Mean Velocity Measurements in Complex Turbulent Flows,” *Exp. Fluids*, **34**(4), pp. 494–503.
- Taylor, C. A., and Draney, M. T., 2004, “Experimental and Computational Methods in Cardiovascular Fluid Mechanics,” *Annu. Rev. Fluid Mech.*, **36**, pp. 197–231.
- Marshall, I., Zhao, S. Z., Papatathanasopoulou, P., Hoskins, P., and Xu, X. Y., 2004, “MRI and CFD Studies of Pulsatile Flow in Healthy and Stenosed Carotid Bifurcation Models,” *J. Biomech.*, **37**(5), pp. 679–687.
- Elkins, C. J., and Alley, M. T., 2007, “Magnetic Resonance Velocimetry: Applications of Magnetic Resonance Imaging in the Measurement of Fluid Motion,” *Exp. Fluids*, **43**(6), pp. 823–858.
- Vennemann, P., Lindken, R., and Westerweel, J., 2007, “In Vivo Whole-Field Blood Velocity Measurement Techniques,” *Exp. Fluids*, **42**(4), pp. 495–511.
- Bonn, D., Rodts, S., Groeninck, M., Rafai, S., Shahidzadeh-Bonn, N., and Coussot, P., 2008, “Some Applications of Magnetic Resonance Imaging in Fluid Mechanics: Complex Flows and Complex Fluids,” *Annu. Rev. Fluid Mech.*, **40**, pp. 209–233.
- Lindemann, J., Keck, T., Wiesmiller, K., Sander, L., Brambs, H. J., Rettinger, G., and Pless, D., 2004, “A Numerical Simulation of Intranasal Air Temperature During Inspiration,” *Laryngoscope*, **114**(6), pp. 1037–1041.
- Pless, D., Keck, T., Wiesmiller, K., Rettinger, G., Aschoff, A. J., Fleiter, T. R., and Lindemann, J., 2004, “Numerical Simulation of Air Temperature and Airflow Patterns in the Human Nose During Expiration,” *Clin. Otolaryngol.*, **29**(6), pp. 642–647.
- Lindemann, J., Keck, T., Wiesmiller, K., Sander, B., Brambs, H. J., Rettinger, G., and Pless, D., 2006, “Nasal Air Temperature and Airflow During Respiration in Numerical Simulation Based on Multislice Computed Tomography Scan,” *Am. J. Rhinol.*, **20**(2), pp. 219–223.
- Kimbell, J. S., Gross, E. A., Joyner, D. R., Godo, M. N., and Morgan, K. T., 1993, “Application of Computational Fluid Dynamics to Regional Dosimetry of Inhaled Chemicals in the Upper Respiratory Tract of the Rat,” *Toxicol. Appl. Pharmacol.*, **121**(2), pp. 253–263.
- Kimbell, J. S., Godo, M. N., Gross, E. A., Joyner, D. R., Richardson, R. B., and Morgan, K. T., 1997, “Computer Simulation of Inspiratory Airflow in All Regions of the F344 Rat Nasal Passages,” *Toxicol. Appl. Pharmacol.*, **145**(2), pp. 388–398.
- Kimbell, J. S., Subramaniam, R. P., Gross, E. A., Schlosser, P. M., and Morgan, K. T., 2001, “Dosimetry Modeling of Inhaled Formaldehyde: Comparisons of Local Flux Predictions in the Rat, Monkey, and Human Nasal Passages,” *Toxicol. Sci.*, **64**(1), pp. 100–110.
- Kepler, G. M., Richardson, R. B., Morgan, K. T., and Kimbell, J. S., 1998, “Computer Simulation of Inspiratory Nasal Airflow and Inhaled Gas Uptake in a Rhesus Monkey,” *Toxicol. Appl. Pharmacol.*, **150**(1), pp. 1–11.
- Subramaniam, R. P., Richardson, R. B., Morgan, K. T., Kimbell, J. S., and Guilmette, R. A., 1998, “Computational Fluid Dynamics Simulations of Inspiratory Airflow in the Human Nose and Nasopharynx,” *Inhalation Toxicol.*, **10**(5), pp. 473–502.
- Minard, K. R., Einstein, D. R., Jacob, R. E., Kabilan, S., Kuprat, A. P., Timchalk, C. A., Trease, L. L., and Corley, R. A., 2006, “Application of Magnetic Resonance (MR) Imaging for the Development and Validation of Computational Fluid Dynamic (CFD) Models of the Rat Respiratory System,” *Inhalation Toxicol.*, **18**(10), pp. 787–794.
- Keyhani, K., Scherer, P. W., and Mozell, M. M., 1995, “Numerical Simulation of Airflow in the Human Nasal Cavity,” *ASME J. Biomech. Eng.*, **117**(4), pp. 429–441.
- Keyhani, K., Scherer, P. W., and Mozell, M. M., 1997, “A Numerical Model of Nasal Odorant Transport for the Analysis of Human Olfaction,” *J. Theor. Biol.*, **186**(3), pp. 279–301.
- Zhao, K., Scherer, P. W., Hajiloo, S. A., and Dalton, P., 2004, “Effect of Anatomy on Human Nasal Air Flow and Odorant Transport Patterns: Implications for Olfaction,” *Chem. Senses*, **29**(5), pp. 365–379.
- Zhao, K., Dalton, P., Yang, G. C., and Scherer, P. W., 2006, “Numerical Modeling of Turbulent and Laminar Airflow and Odorant Transport During Sniffing in the Human and Rat Nose,” *Chem. Senses*, **31**(2), pp. 107–118.
- Yang, G. C., Scherer, P. W., Zhao, K., and Mozell, M. M., 2007, “Numerical Modeling of Odorant Uptake in the Rat Nasal Cavity,” *Chem. Senses*, **32**(3), pp. 273–284.
- Yang, G. C., Scherer, P. W., and Mozell, M. M., 2007, “Modeling Inspiratory and Expiratory Steady-State Velocity Fields in the Sprague-Dawley Rat Nasal Cavity,” *Chem. Senses*, **32**(3), pp. 215–223.
- Negus, V. E., 1958, *The Comparative Anatomy and Physiology of the Nose and Paranasal Sinuses*, Livingstone, London.
- Freitas, C., 1993, “Journal of Fluids Engineering Editorial Policy Statement on the Control of Numerical Accuracy,” *ASME J. Fluids Eng.*, **115**, pp. 339–340.
- Shi, H., Kleinstreuer, C., and Zhang, Z., 2006, “Laminar Airflow and Nanoparticle or Vapor Deposition in a Human Nasal Cavity Model,” *ASME J. Biomech. Eng.*, **128**, pp. 697–706.
- Shi, H., Kleinstreuer, C., and Zhang, Z., 2007, “Modeling of Inertial Particle Transport and Deposition in Human Nasal Cavities With Wall Roughness,” *J. Aerosol Sci.*, **38**(4), pp. 398–419.
- Liu, Y., Matida, E. A., Gu, J., and Johnson, M. R., 2007, “Numerical Simulation of Aerosol Deposition in a 3-D Human Nasal Cavity Using RANS, RANS/EIM, and LES,” *J. Aerosol Sci.*, **38**(7), pp. 683–700.
- Xi, J., and Longest, P. W., 2008, “Numerical Predictions of Submicrometer Aerosol Deposition in the Nasal Cavity Using a Novel Drift Flux Approach,” *Int. J. Heat Mass Transfer*, **51**, pp. 5562–5577.
- Xi, J., Longest, P., and Martonen, T. B., 2008, “Effects of the Laryngeal Jet on Nano- and Microparticle Transport and Deposition in an Approximate Model

- of the Upper Tracheobronchial Airways,” *J. Appl. Physiol.*, **104**(6), pp. 1761–1777.
- [43] Longest, P. W., and Vinchurkar, S., 2007, “Effects of Mesh Style and Grid Convergence on Particle Deposition in Bifurcating Airway Models With Comparisons to Experimental Data,” *Med. Eng. Phys.*, **29**(3), pp. 350–366.
- [44] Vinchurkar, S., and Longest, P. W., 2008, “Evaluation of Hexahedral, Prismatic and Hybrid Mesh Styles for Simulating Respiratory Aerosol Dynamics,” *Comput. Fluids*, **37**(3), pp. 317–331.
- [45] Roache, P. J., 1998, *Verification and Validation in Computational Science and Engineering*, Hermosa, Albuquerque, NM.
- [46] Roache, P. J., Ghia, K. N., and White, F. M., 1986, “Editorial Policy Statement on the Control of Numerical Accuracy,” *ASME J. Fluids Eng.*, **108**(1), p. 2.
- [47] Craven, B. A., Neuberger, T., Paterson, E. G., Webb, A. G., Josephson, E. M., Morrison, E. E., and Settles, G. S., 2007, “Reconstruction and Morphometric Analysis of the Nasal Airway of the Dog (*Canis Familiaris*) and Implications Regarding Olfactory Airflow,” *Anat. Rec.*, **290**(11), pp. 1325–1340.
- [48] Madasu, S., Borhan, A., and Ultman, J. S., 2006, “An Axisymmetric Single-Path Model for Gas Transport in the Conducting Airways,” *ASME J. Biomech. Eng.*, **128**(1), pp. 69–75.
- [49] Gedeon, D., 1986, “Mean-Parameter Modeling of Oscillating Flow,” *ASME J. Heat Transfer*, **108**(3), pp. 513–518.
- [50] Elad, D., Liebenthal, R., Wenig, B. L., and Einav, S., 1993, “Analysis of Air Flow Patterns in the Human Nose,” *Med. Biol. Eng. Comput.*, **31**(6), pp. 585–592.
- [51] Naftali, S., Schroter, R. C., Shiner, R. J., and Elad, D., 1998, “Transport Phenomena in the Human Nasal Cavity: A Computational Model,” *Ann. Biomed. Eng.*, **26**(5), pp. 831–839.
- [52] Naftali, S., Rosenfeld, M., Wolf, M., and Elad, D., 2005, “The Air-Conditioning Capacity of the Human Nose,” *Ann. Biomed. Eng.*, **33**(4), pp. 545–553.
- [53] Elad, D., Naftali, S., Rosenfeld, M., and Wolf, M., 2006, “Physical Stresses at the Air-Wall Interface of the Human Nasal Cavity During Breathing,” *J. Appl. Physiol.*, **100**(3), pp. 1003–1010.
- [54] Craven, B. A., 2008, “A Fundamental Study of the Anatomy, Aerodynamics, and Transport Phenomena of Canine Olfaction,” Ph.D. thesis, Pennsylvania State University, University Park, PA.
- [55] Loudon, C., and Tordesillas, A., 1998, “The Use of the Dimensionless Womersley Number to Characterize the Unsteady Nature of Internal Flow,” *J. Theor. Biol.*, **191**(1), pp. 63–78.
- [56] Telionis, D. P., 1981, *Unsteady Viscous Flows*, Springer-Verlag, New York.
- [57] Cimbala, J. M., and Cengel, Y. A., 2008, *Essentials of Fluid Mechanics: Fundamentals and Applications*, McGraw-Hill, New York.
- [58] White, F. M., 2003, *Fluid Mechanics*, McGraw-Hill, New York.
- [59] Peacock, J., Jones, T., Tock, C., and Lutz, R., 1998, “The Onset of Turbulence in Physiological Pulsatile Flow in a Straight Tube,” *Exp. Fluids*, **24**(1), pp. 1–9.
- [60] Peacock, J., Jones, T., Tock, C., and Lutz, R., 1997, “An in Vitro Study on the Effect of Branch Points on the Stability of Coronary Artery Flow,” *Med. Eng. Phys.*, **19**(2), pp. 101–108.
- [61] Tennekes, H., and Lumley, J. L., 1972, *A First Course in Turbulence*, MIT, Cambridge, MA.
- [62] Mathieu, J., and Scott, J., 2000, *An Introduction to Turbulent Flow*, Cambridge University Press, New York.
- [63] Pope, S. B., 2000, *Turbulent Flows*, Cambridge University Press, New York.
- [64] Wilcox, D. C., 1998, *Turbulence Modeling for CFD*, DCW Industries, Inc., La Cañada, CA.
- [65] Ryval, J., Straatman, A. G., and Steinman, D. A., 2004, “Two-Equation Turbulence Modeling of Pulsatile Flow in a Stenosed Tube,” *ASME J. Biomech. Eng.*, **126**, pp. 625–635.
- [66] Varghese, S. S., and Frankel, S. H., 2003, “Numerical Modeling of Pulsatile Turbulent Flow in Stenotic Vessels,” *ASME J. Biomech. Eng.*, **125**, pp. 445–460.
- [67] Varghese, S. S., Frankel, S. H., and Fischer, P. F., 2008, “Modeling Transition to Turbulence in Eccentric Stenotic Flows,” *ASME J. Biomech. Eng.*, **130**, p. 014503.
- [68] Varghese, S. S., Frankel, S. H., and Fischer, P. F., 2007, “Direct Numerical Simulation of Stenotic Flows. Part 1. Steady Flow,” *J. Fluid Mech.*, **582**, pp. 253–280.
- [69] Zhang, Z., and Kleinstreuer, C., 2003, “Low-Reynolds-Number Turbulent Flows in Locally Constricted Conduits: A Comparison Study,” *AIAA J.*, **41**(5), pp. 831–840.
- [70] Kleinstreuer, C., and Zhang, Z., 2003, “Laminar-to-Turbulent Fluid-Particle Flows in a Human Airway Model,” *Int. J. Multiphase Flow*, **29**(2), pp. 271–289.
- [71] Younis, B. A., and Berger, S. A., 2004, “A Turbulence Model for Pulsatile Arterial Flows,” *ASME J. Biomech. Eng.*, **126**, pp. 578–584.
- [72] Proctor, D. F., 1982, “The Mucociliary System,” *The Nose: Upper Airway Physiology and the Atmospheric Environment*, Elsevier Biomedical Press, New York, Chap. 10, pp. 245–278.
- [73] Getchell, T. V., Heck, G. L., Desimone, J. A., and Price, S., 1980, “Location of Olfactory Receptor-Sites—Inferences From Latency Measurements,” *Biophys. J.*, **29**(3), pp. 397–411.
- [74] Reznik, G. K., 1990, “Comparative Anatomy, Physiology, and Function of the Upper Respiratory-Tract,” *Environ. Health Perspect.*, **85**, pp. 171–176.
- [75] Menco, B. P. M., and Farbman, A. I., 1992, “Ultrastructural Evidence for Multiple Mucous Domains in Frog Olfactory Epithelium,” *Cell Tissue Res.*, **270**(1), pp. 47–56.
- [76] Sharc Ltd., 2007, *HARPOON 2.5 User Guide*.
- [77] Biswas, R., and Strawn, R. C., 1998, “Tetrahedral and Hexahedral Mesh Adaptation for CFD Problems,” *Appl. Numer. Math.*, **26**(1–2), pp. 135–151.
- [78] Shakib, F., 1989, “Finite Element Analysis of the Compressible Euler and Navier–Stokes Equations,” Ph.D. thesis, Stanford University, Stanford, CA.
- [79] Hughes, T. J. R., Franca, L. P., and Hulbert, G. M., 1989, “A New Finite Element Formulation for Computational Fluid Dynamics: VIII. The Galerkin/Least-Squares Method for Advective-Diffusive Equations,” *Comput. Methods Appl. Mech. Eng.*, **73**(2), pp. 173–189.
- [80] ACUSIM Software, Inc., 2007, *AcuSolve 1.7 Reference Manual*.
- [81] Lyons, D. C., Peltier, L. J., Zajackowski, F. J., and Paterson, E. G., 2008, “Assessment of DES Models for Separated Flow From a Hump in a Turbulent Boundary Layer,” *ASME J. Fluids Eng.*, in press.
- [82] Roache, P. J., 1994, “Perspective—A Method for Uniform Reporting of Grid Refinement Studies,” *ASME J. Fluids Eng.*, **116**(3), pp. 405–413.